density, and mass density[3,4,5] than that acquired by conventional scanners. Furthermore, the monochromatic X-ray image acquired by the dual-energy scanner theoretically yields more accurate data than that of the conventional scanner because the theory (details in the paragraph below) predicts the elimination of spectral beam hardening artifacts.[5,6,7] We reasoned that the monochromatic image could make more accurate dose distribution calculations when applied to radiotherapy treatment planning (RTP). Therefore, we set out to validate this technique.

There are three types of dual-energy CT acquisition systems commercially available: Toshiba (Toshiba Corporation, Tokyo, Japan) with one tube and two rotations, Siemens[8] (Siemens Medical Solutions, Malvern, PA, USA) with two tubes and one rotation, and GE[9] (GE Healthcare, Waukesha, WI, USA) with one tube one rotation called a fast switching system. The similar system to that from GE is described in several papers.[7,10,11] One of the most important requirements for the success of dual-energy CT scanning is that there should be minimal time delay between the two acquisitions of the two single energy projection/images. We utilize a Discovery CT750 HD (GE Healthcare). In the GE system, fast rotation speed (0.5–1 s), use of X-ray focal spot deflection, fast voltage switching speed between 80 and 140 kVp in less than 0.5 ms, and a newly developed cerium activated garnet rare-earth composite scintillator detector with 100 times faster response than a typical gadolinium oxysulfide CT detector allow us to perform successful dual-energy CT acquisition.

The basic theory of this algorithm was first reported by Alvarez and Macovski[6] and studied extensively by others.[12,13] The system uses a dual-energy pre-reconstruction algorithm for creating synthesized monochromatic CT image from the material density images. The following is an explanation of the method.[7,9] The basic assumption underlying this algorithm is that over the diagnostic X-ray energy range, the explicitly energy-dependent linear attenuation coefficient of all materials can be expressed with sufficient accuracy as a linear combination of photoelectric and Compton coefficients.[6] In direct consequence, the linear attenuation coefficient in each voxel of CT image at energy, E, is given by:

$$\mu^{L}(E) = d_{\alpha} \cdot \mu^{M}(E)_{\alpha} + d_{\beta} \cdot \mu^{M}(E)_{\beta}$$

(1)

where $\mu^{L}(E)$ is linear attenuation coefficient in each voxel at X-ray energy E (in kVp), and d_{α} and d_{β} are the dual-energy CT determined densities or concentrations of basis materials α and β at the voxel location, respectively. Thus, the information of two materials is needed to calculate the linear attenuation coefficient. It should be sufficiently different in their atomic number Z and in their photoelectric and Compton attenuation characteristics to distinguish the two materials. $\mu^{M}(E)_{\alpha}$ and $\mu^{M}(E)_{\beta}$ are the mass attenuation coefficients of material α and β. In CT, the line integral over the linear attenuation coefficient $\int \mu^{L}(r, E)ds$ is determined for each focus position and detector element, respectively. This integral can be expressed accordingly as:

$$\int \mu^{L}(r,E)ds = \delta_{\alpha} \cdot \mu^{M}(E)_{\alpha} + \delta_{\beta} \cdot \mu^{M}(E)_{\beta}$$

(2)

where

$$\delta_{i} = \int d_{i}(r)ds$$

(3)

δ_{i} is the area density in g/cm^2 and $d_{i}(r)$ is the local density in g/cm^3 of the basis material i.

The equivalent area densities, δ_α and δ_β, are determined for each ray path in projections. This problem is solved by measuring the attenuation with two different energies (spectra). Because the X-ray attenuates according to Beer-Lambert law (i.e., exponential attenuation law):

$$I = I_0(E) \cdot \exp\left[-\int \mu^L(r,E)ds \right] \tag{4}$$

where I and I_0 are the attenuated and primary intensities, two nonlinear equations for each path are derived:

$$I_h = I_{0h}(E) \cdot \exp\left[-\delta_\alpha \cdot \mu^M(E)_\alpha - \delta_\beta \cdot \mu^M(E)_\beta \right]dE \tag{5}$$

$$I_l = I_{0l}(E) \cdot \exp\left[-\delta_\alpha \cdot \mu^M(E)_\alpha - \delta_\beta \cdot \mu^M(E)_\beta \right]dE \tag{6}$$

The subscripts h and l refer to the high- and low-kVp energy. Eqs. (5) and (6) can be solved for the equivalent area densities, δ_α and δ_β.

Since mass attenuation coefficient would have been measured with a mono-energetic X-ray source,[14] once the equivalent area densities are determined, the projection data can be calculated. This is done by multiplying the known area density values by the mass attenuation coefficients of the respective basis materials for an arbitrary mono-energy E_0 (in keV):

$$\int \mu^L(r,E_0)ds = \delta_\alpha \cdot \mu^M(E_0)_\alpha + \delta_\beta \cdot \mu^M(E_0)_\beta \tag{7}$$

where $\mu^M(E_0)_i$ are taken from Storm and Israel.[14] The projection data are then subjected to the standard reconstruction process yielding CT images in Hounsfield units (HU).[15]

In conventional CT, the HU or CT number (CT#) is computed as:

$$CT\#(E) = \frac{\mu^L(E) - \mu^L(E)_w}{\mu^L(E)_w} \cdot 1000 \tag{8}$$

where $\mu^L(E)_w$ is the linear attenuation of pure water at a given energy E. In dual-energy CT, to calculate $CT\#$ at E_0, the equation is transformed using the linear mass relationship $\mu^L = \rho\mu^M$ and substituted Eq. (1) into Eq. (8):

$$CT\#(E_0) = \frac{d_\alpha \cdot \mu^M(E_0)_\alpha + d_\beta \cdot \mu^M(E_0)_\beta - \rho_w \cdot \mu^M(E_0)_w}{\rho_w \cdot \mu^M(E_0)_w} \cdot 1000 \tag{9}$$

where ρ_w and $\mu^M(E_0)_w$ are the pure water mass density and mass attenuation coefficient of pure water at energy E_0, respectively. This monochromatic image synthesis workflow is implemented in Gemstone spectral imaging (GSI) mode while standard polychromatic images were obtained using the regular operation mode.

The goal of this study is to provide CT to ED (electron density) conversion curves derived from dual-energy CT monochromatic images for RTP. The CT number accuracy, as well as the reproducibility of CT numbers (an important factor on quality assurance), was also investigated.

II. MATERIALS AND METHODS

A. Phantom

A tissue characterization phantom (Gammex RMI 467, Gammex RMI, Middleton, WI, USA) with 33 cm in diameter and 5 cm in height was used. The rods' compositions mimicked those of human body organs with known electron densities relative to water, ranging from low (e.g., air) to high (e.g., bone). The phantom was composed mainly of solid water. In radiotherapy, this phantom is commonly used to establish EDs of various tissues and their corresponding CT numbers (in Hounsfield units, HU) for accurate corrections for tissue heterogeneity. Table 1 summarizes the physical characteristics of the rods (provided by the manufacturer to compensate slight differences among products). Correctly aligning rods is quite important because high-density rods cause artifacts that affect the accuracy of the CT numbers. Therefore, rods were inserted into the phantom according to the manufacture's recommendations (Tissue Characterization Phantom Model 467 User's Guide).[16] Figure 1 shows the distribution of the rods used in this study.

TABLE 1. Physical characteristics of rods. The data are listed in ascending order by electron density.

| Rod Material	Electron Density Relative to Water	Physical Density (g/cm³)
LN-300 Lung	0.284	0.290
LN-450 Lung	0.445	0.460
AP6 Adipose	0.924	0.941
BR-12 Breast	0.957	0.980
CT Solid Water	0.988	1.017
Water Insert	1.000	1.000
BRN-SR2 Brain	1.049	1.053
LV1 Liver	1.062	1.094
IB Inner Bone	1.097	1.144
B200 Bone Mineral	1.096	1.143
CB2-30% $CaCO_3$	1.279	1.334
CB2-50% $CaCO_3$	1.470	1.560
SB3 Cortical Bone	1.696	1.824
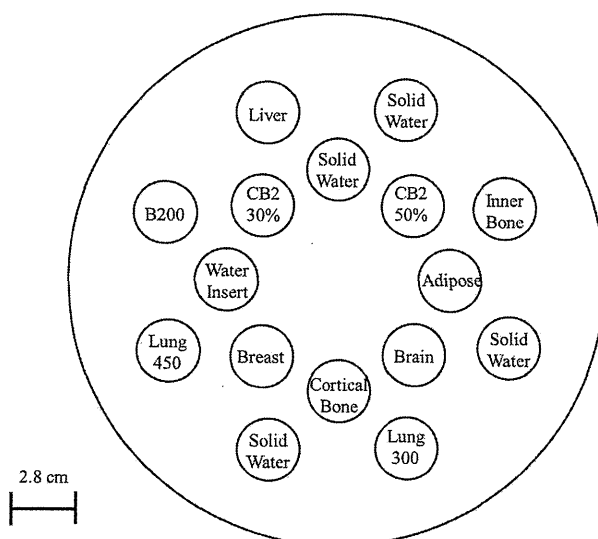
FIG. 1. Phantom rod alignment. The high-density materials were positioned to minimize artifacts.

B. Measurements

The phantom was carefully placed at the isocenter of the gantry using well-coordinated laser pointer system to ensure that the central axis and transverse plane of the phantom were precisely on the longitudinal axis and imaging plane, respectively. Since helical scanning was typically used in the CT simulation for RTP, all measurements were acquired by helical scanning in either Regular or GSI mode. Table 2 summarizes the scan parameters. The standard 120 kVp image was reconstructed using Regular mode with the parameters listed in Table 3. The monochromatic images at 60 keV (relatively lower setting), 77 keV, 100 keV, and 140 keV (the highest setting) were reconstructed using GSI mode with the parameters listed in Table 3, where 77 keV is approximately equal to the effective energy of a 120 kVp polychromatic X-ray beam, according to the scanner specifications.

Furthermore, the reproducibility of CT number was validated over "short" ($\leq$ 24 h) and "long" (~ 1 month) time periods, which were every two hours from 9 a.m. to 5 p.m., or once a week, respectively. Each scan was performed once.

TABLE 2. Scan parameters.

Mode	Scan	kVp	mA	Rotation Time (s)	SFOV	Slice Thickness (mm)	Beam Collimation (mm)
Regular	Helical	120	630	0.5	Large body	2.5	40
GSI	Helical	80/140	600	1.0	Large body	2.5	40

SFOV = scan field of view.

TABLE 3. Reconstruction parameters of the two imaging modes.

Mode	DFOV (cm)	Recon Kernel	Energy
Regular	50	Standard	N/A
GSI	50	Standard	Mono 60-140 keV

DFOV = display field of view, N/A = not applicable.

C. Data analysis

The region of interest (ROI) measurement for each phantom rod was delineated using ImageJ software.[17] Images at the center slice were analyzed. The ROI diameter was approximately 1.9 cm and its size was slightly smaller than that of the rod. Solid water-rod CT numbers are represented by the average for the four rods in the phantom.

We first plotted the measured CT number for each material against the monochromatic imaging energy. Second, the reproducibility of the CT data for each material and monochromatic imaging energy was evaluated by using their standard deviation at short and long time periods, as indicated above. Two-sided 68% confidence intervals were used to assess precision. Third, we plotted relative ED as a function of CT number.

The true CT numbers of the rods inserted in the phantom at each energy were computed from the mass attenuation coefficients using NIST XCOM computer program,[18,19] and the mass densities are shown in Table 1. The material composition of the inserts used in the program is provided by the manufacture. The program uses the following equation:

$$CT\#(E_0)_j = \frac{\rho_j \cdot \mu^M (E_0)_j - \rho_w \cdot \mu^M (E_0)_w}{\rho_w \cdot \mu^M (E_0)_w} \cdot 1000 \tag{10}$$

where ρ_j and $\mu^M(E_0)_j$ are the mass density of material j and mass attenuation coefficient of the material at energy E_0, respectively. At room temperature, 0.99823 g/cm^3 at 20°C was used as water mass density.

III. RESULTS

A. Differences in CT number with different combinations of materials and monochromatic imaging energies

Figure 2 presents the CT images acquired by scanning in both modes. The 60 keV image contains an artifact appearing as a dark band around the cortical bone rod (Fig. 2(b), arrow). The magnitude of this artifact was reduced as monochromatic image energy increased. However,
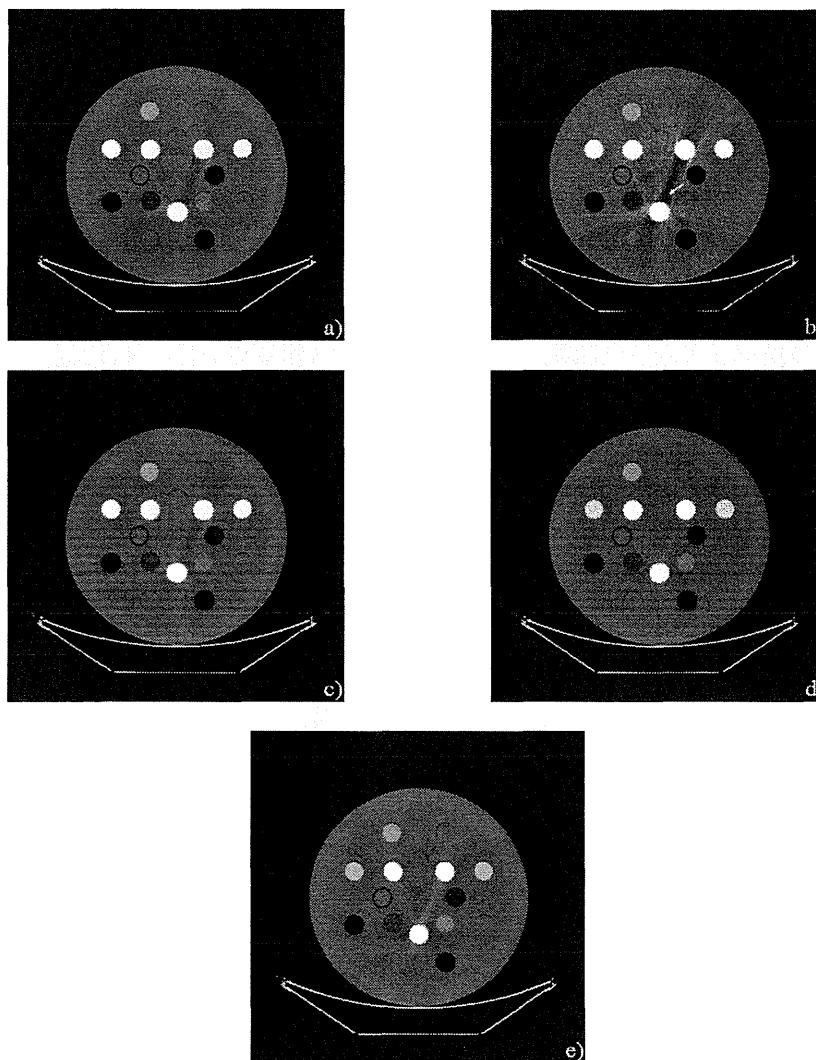

FIG. 2. Overview of polychromatic and monochromatic images: a) 120 kVp, b) 60 keV, c) 77 keV, d) 100keV, e) 140 keV. The arrow indicates an artifact appearing as a dark band around the cortical bone rod.

a slight artifact around the rod was observed at 140 keV. The image at 100 keV was visibly better in quality in this study.

The CT number changed dramatically for high-density material rods as shown by the monochromatic images in Fig. 3. However, the CT number varied little in the materials with densities less than or equal to water, and CT number differences for high-energy images were less than those of lower energy images for the various material regions. The CT number range at 140 keV was about 1470 HU compared with 2300 HU at 60 keV, and was approximately 1.5-fold smaller at high energies.
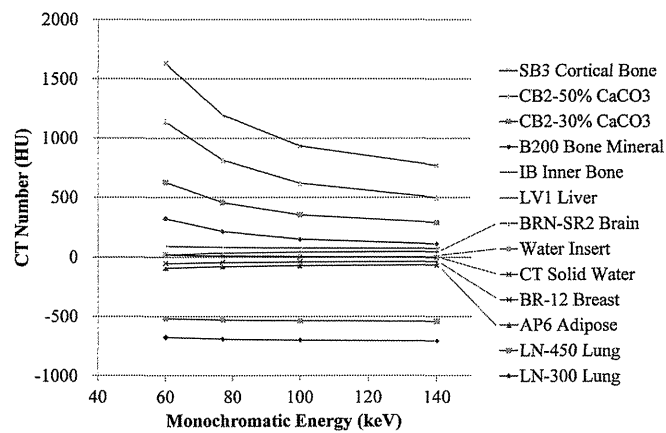

FIG. 3. Distribution of CT number among materials as a function of monochromatic energy.

B. CT number reproducibility over a short time period

Figure 4 shows standard deviations of the CT numbers over a short time period. The standard deviation at 120 kVp was close to that at 77 keV (-7.48 ± -1.56 HU, the difference averaged for all materials) and was also small at high energies: 140 keV, CB2-50% = 2.7 HU. In contrast, this number was greater at low energies: 60 keV, CB2-50% = 22.8 HU.
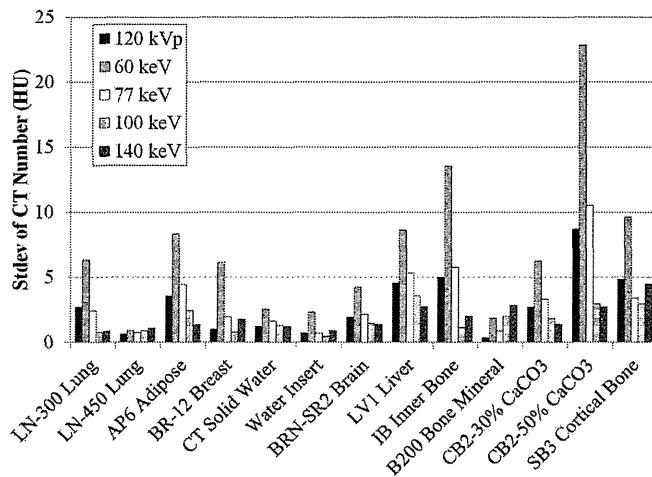

FIG. 4. Standard deviations of CT numbers over a short time period.

C. CT number reproducibility over a long time period

Figure 5 shows standard deviations for CT numbers over a long time period. The trend was similar to that for a short time period, as stated above.
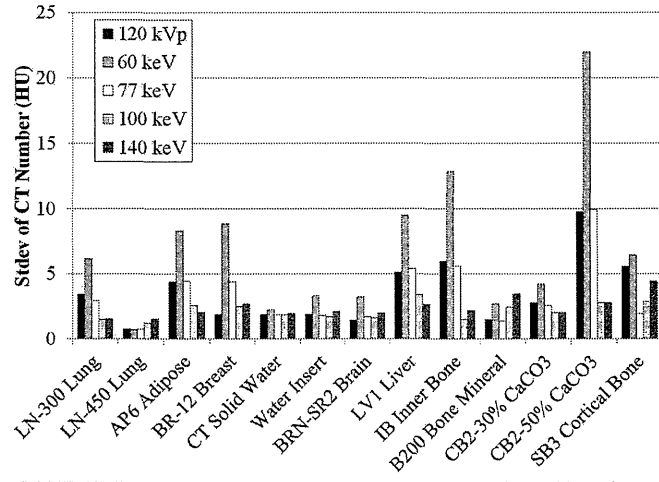

FIG. 5. Standard deviations of CT numbers over a long time period.

D. CT number differences between monochromatic image and theoretical value

The CT number accuracy of the inserts was investigated. Figure 6 shows CT number difference between monochromatic image and theoretical (true) value in soft tissues. As the energy increases, the difference is smaller. The 140 keV monochromatic image had the least amount of CT number deviation among the materials. Figure 7 shows differences between monochromatic image and theoretical (true) CT number values in bony materials. The difference is less in images at higher energy. In SB3 cortical bone, the CT number is dramatically affected by the energy increases.
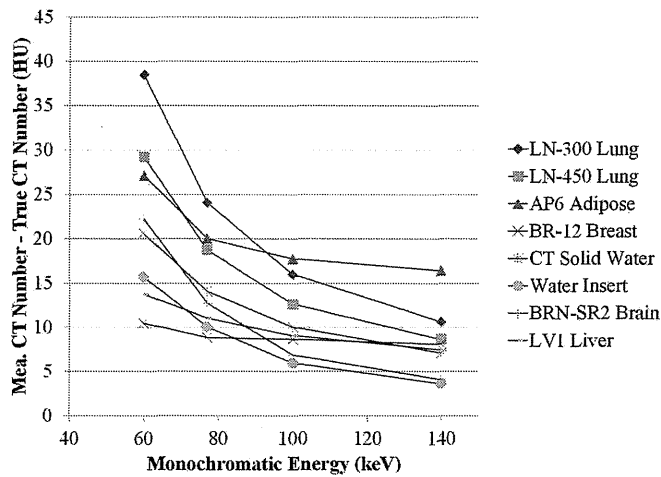

FIG. 6. CT number difference between monochromatic image (measured) and theoretical (true) value in soft tissues.
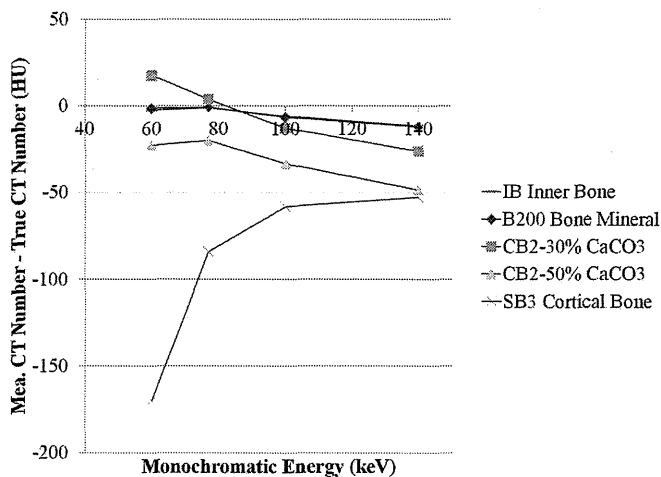

FIG. 7. CT number difference between monochromatic image (measured) and theoretical (true) value in bony materials.

E.   CT number to ED conversion curves for monochromatic images

Figure 8 shows the CT to ED conversion curves for various monochromatic images. These curves were generated from the short time period data. The curves plotted from the data for long time periods exhibited the similar trend and are, therefore, not presented here. The standard CT image curve displayed a bilinear relationship clustering around 0 HU (Fig. 8). There were no significant differences between the curves at numbers < water (0 HU). The curves' shapes at 77 keV and 120 kVp were similar. The bilinear relationship gradually diminished with increasing energy. The curve for 140 keV was nearly linear.
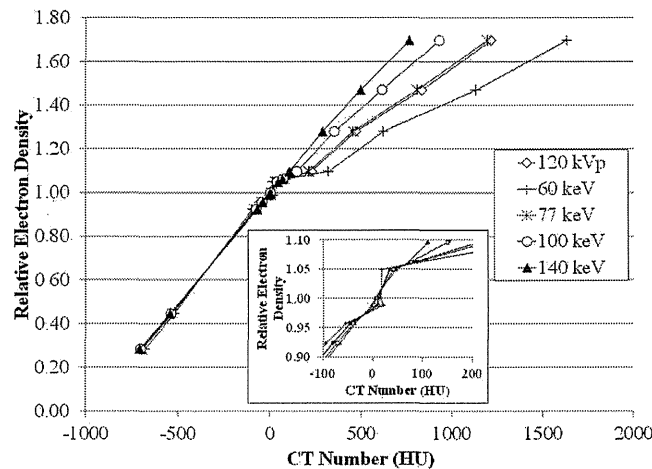

FIG. 8. CT to ED conversion curves obtained by monochromatic images. The cutout shows the plots around 0 HU.

IV. DISCUSSION

Dual-energy CT provides clinically useful, material-specific information[9] in addition to the morphological information.[20,21] As a first step on the application of dual-energy CT for RTP, we evaluated the CT numbers of ED-known materials on monochromatic images obtained by the GSI operation mode.

In the GSI mode, the "monochromatic image" is reconstructed from "monochromatic projections", which are calculated from 80 kVp and 140 kVp projections. In other words, the monochromatic image is not obtained with monochromatic X-ray projections, but "synthesized" with polychromatic 80 kVp and 140 kVp X-ray projections. It should be noted that the lowest energy (e.g., 60 keV) monochromatic image is predominantly derived from 80 kVp projections than 140 kVp ones. It is well known that lower energy X-rays are attenuated to a greater extent than higher energy X-rays when a polychromatic X-ray beam, especially one generated with a low tube voltage, passes through an object being imaged. This so-called beam hardening phenomenon[22] induces dark (or white) band artifacts because X-rays from some projection angles are hardened to a differing extent than rays from other angles. This confuses the reconstruction algorithm. The most common example occurs between the dense materials, and is demonstrated in Fig. 2(a) from 120 kVp imaging. This phenomenon could be theoretically suppressed with a "true" monochromatic X-ray, but remains in the "synthesized" monochromatic image, especially at a lower energy (Fig. 2(b)). Goodsitt et al.[23] also reported that the synthesized monochromatic images are not truly monochromatic, especially at lower energy. This is partly due to the scattering X-rays from outside the focal spot or surrounding material. The theory is not able to take into account the scatter effect while addressing the beam

hardening effect. The scatter effect on dual-energy CT was studied by Vetter and Holden.[24] They found about 2% variations under different measurement conditions, and demonstrated nonlinearities in lookup tables due to the scatter effect. Their scanner had a collimator of 10 mm width. However, the GE scanner in this experiment used a 20 to 40 mm width. As a result, the scanner suffers from the scatter effect due to higher scatter fractions. In addition, the scatter fraction changes with each energy.[24] Implementing better scatter correction algorithms,[25] as well as increasing spectral separation between the low- and high-energy X-ray,[4,26,27] could improve the synthesized monochromatic image.

To our knowledge, there have been few reports using the GE scanner to study the CT number of various materials except for water.[23,28] The CT number changed dramatically for high-density materials in the different monochromatic images (Fig. 3). This result is consistent with data acquired using iodine solutions.[28] The high degree of change in CT numbers is caused by the dominance of the photoelectric effect over that of the Compton effect. The photoelectric effect probability at low energy is proportional to the atomic number cubed. In contrast, the Compton effect becomes dominant as the photon energy increases and is independent of atomic number. Therefore, the CT number varies little among diverse types of materials at high energy and explains why the CT number range is small for high-energy images.

CT number reproducibility during short and long time periods is quite important for any application using the CT number, such as the RTP system. To our knowledge, there are no reports of the stability over a day or a month. The stability of CT number of any materials is investigated only over the short term.[23,28] The trend of the CT number reproducibility was the same over a short or long time period, thus confirming the scanner stability. However, the standard deviation was somewhat large for CB2-50% at 60 keV. We consider that this might be due to the streak artifact reported by Papanikolaou et al.[29] This artifact would be, as described above, due to the fact that the image is not truly monochromatic. The artifact extended in a direction toward the CB2-50% rod (Fig. 2(b)). The artifact was reduced as the energy used to generate the monochromatic image was increased. This would explain the stability of CT number at the CB2-50% rod (Figs. 4 and 5). Although the large standard deviation may also result from noise on the 60 keV image, the noise is comparatively lower, as reported by Zhang et al.,[28] and would not primarily affect the standard deviation.

Image noise for given dose is also an important property. The noise determines the lower limit of subject contrast that can be distinguished by the observer. Less noise image would have more benefit for contouring objects, as well as dose calculation, in RTP. Theory predicts that there is an optimal energy for which the noise in the monochromatic energy has the same energy as in a regular CT, for the same given dose.[13] A study using a water-equivalent uniform phantom shows that the monochromatic images at the optimal energy have higher noise level than diagnostic X-ray energy range under the same acquisition and reconstruction conditions.[28] In our experiment (data not shown), in the monochromatic image the standard deviation within the ROI of the water insert showed a similar trend to previous studies — the noise dramatically decreases to the optimal energy and gradually increases as the energy increases.[13,28] The other inserts also showed a similar variation as the water insert. The noise of all inserts was also consistent over both short and long time periods. The noise is a very sensitive parameter to the overall imaging performance of the scanner. The scanner stability was also confirmed from this point of view.

An accurate dose calculation algorithm, as well as accurate determination of the relationship between CT number and ED, is required to accurately calculate dose distribution, minimizing discrepancy between calculated and actual dose. Venselaar et al.[30] reported tolerances for the accuracy of RTP dose calculations. The accuracies required for dose calculations for homogeneous and heterogeneous media are 2% and 3%, respectively.[30] The 20 HU change in the CT number for soft tissues and 250 HU for bone result in about 1% of change for monitor unit (MU) for a brain case and 2% change for a lung and pelvis case.[29] The results could be transferred into the dose calculation in monochromatic image because the CT number is

normalized to water. In our experiment, the results show such changes in monochromatic images at lower energy (e.g., 60 keV) between measured and true value in several tissues, but not in bony materials (Figs. 6 and 7). CT number stability results also compensate the accuracy. The study, however, shows larger difference below 60 keV in soft tissue and bone than the criteria described above (i.e., 20 HU for soft tissue and 250 HU for bone).[23] That implies that the dose calculation on monochromatic images lower than 60 keV would result in larger dosimetric differences compared with other energies. The other important factor for the dose calculation is the phantom (body) size because size changes the X-ray attenuation, as well as the amount of scatter from surrounding material, resulting in CT number change. The size has a high impact on CT number.[31] Bone CT numbers under several composition variations considerably differ between small and large phantom size on monochromatic image at each energy.[23] A phantom of proper size, which is close to a subsequently irradiated part such as head or body, should be scanned.

The CT to ED conversion curves with monochromatic images were determined for RTP. A linear relationship was observed at 140 keV, while the curves in the low-energy image were bilinear, bordering around 0 HU (Fig. 8). At high energies, the Compton effect is dominant over the photoelectric effect, similar to that of megavoltage cone beam CT (MVCBCT).[32] However, the dose calculation for MVCBCT has proven not to be practical because of problems, such as cupping artifacts.[33] Reflecting the Compton effect compared with standard CT images used clinically for CT simulation would predict that dose calculation is performed more accurately using high-energy monochromatic images without the problems associated with MVCBCT.[33] Dosimetric investigation is required for the further evaluation of the dose calculation accuracy with these CT to ED conversion curves.

V.   CONCLUSIONS

This is the first report regarding the CT to ED conversion curves for RTP by a CT scanner with a fast kVp switching system. We present here CT to ED conversion curves acquired from monochromatic images for RTP, assessing CT number accuracy. Reproducibility was confirmed by determining the variation in CT number.

ACKNOWLEDGMENTS

REFERENCES

1. Aird E, Conway J. CT simulation for radiotherapy treatment planning. Br J Radiol. 2002;75(900):937–49.
2. Hounsfield GN. Computerized transverse axial scanning (tomography): Part 1. Description of system. Br J Radiol. 1973;46(552):1016–22.
3. Rutherford RA, Pullan BR, Isherwood I. Measurement of effective atomic number and electron density using an EMI scanner. Neuroradiology. 1976;11(1):15–21.
4. Rutherford RA, Pullan BR, Isherwood I. X-ray energies for effective atomic number determination. Neuroradiology. 1976;11(1):23–28.
5. Brooks RA. A quantitative theory of the Hounsfield unit and its application to dual energy scanning. J Comput Assist Tomogr. 1977;1(4):487–93.
6. Alvarez RE and Macovski A. Energy-selective reconstructions in X-ray computerized tomography. Phys Med Biol. 1976;21(5):733–44.
7. Kalender WA, Perman W, Vetter J, Klotz E. Evaluation of a prototype dual-energy computed tomographic apparatus. I. Phantom studies. Med Phys. 1986;13(3):334–39.

8. Maass C, Baer M, Kachelriess M. Image-based dual energy CT using optimized precorrection functions: a practical new approach of material decomposition in image domain. Med Phys. 2009;36(8):3818–29.

9. Santamaria-Panga A, Duttab S, Makrogiannisc S, et al. Automated liver lesion characterization using fast kVp switching dual energy computed tomography imaging. In: Karssemeijer N and Summers RM, editors. Medical Imaging 2010: Computer Aided Diagnosis. Proc of SPIE 2010;7624.

10. Vetter J, Perman W, Kalender WA, Mazess R, Holden J. Evaluation of a prototype dual-energy computed tomographic apparatus. II. Determination of vertebral bone mineral content. Med Phys. 1986;13(3):340–43.

11. Montner SM, Lehr JL, Oravez WT. Quantitative evaluation of a dual energy CT system. J Comput Assist Tomogr. 1987;11(1):144–50.

12. Lehmann L, Alvarez R, Macovski A, et al. Generalized image combinations in dual KVP digital radiography. Med Phys. 1981;8(5):659–67.

13. Alvarez R, Seppi E. A comparison of noise and dose in conventional and energy selective computed tomography. Nuclear Science, IEEE Transactions on. 1979;26(2):2853–56.

14. Storm E and Israel HI. Photon cross sections from 1 keV to 100 MeV for elements Z = 1 to Z = 100. Los Alamos, NM: Los Alamos Scientific Laboratory; 1970.

15. Slaney M and Kak A. Principles of computerized tomographic imaging. Philadelphia, PA: SIAM; 1988.

16. Gammex Inc. Tissue characterization phantom Gammex 467 user's guide [cited 2012 12/20]. Available from: http://www.gammex.com/n-portfolio/productpage.asp?id=283&category=Radiation+Oncology&name=Tissue+Characterization+Phantom%2C+Gammex+467

17. Abràmoff MD, Magalhães PJ, Ram SJ. Image processing with ImageJ. Biophotonics International. 2004;11(7):36–42.

18. Berger M, Hubbell J, Seltzer S, et al. XCOM: photon cross sections database, NIST standard reference database 8 (XGAM). 2005. Available from: http://www.nist.gov/pml/data/xcom/index.cfm

19. Hubbell JH. Photon cross sections, attenuation coefficients, and energy absorption coefficients from 10 keV to 100 GeV. NSRDS–NBS29. Washington, DC: NIST; 1969.

20. Neville AM, Gupta RT, Miller CM, Merkle EM, Paulson EK, Boll DT. Detection of renal lesion enhancement with dual-energy multidetector CT. Radiology. 2011;259(1):173–83.

21. Lv PJ, Lin XZ, Li JY, Li WX, Chen KM. Differentiation of small hepatic hemangioma from small hepatocellular carcinoma: recently introduced spectral CT method. Radiology. 2011;259(3):720–29.

22. Bushberg JT, Seibert JA, Leidholdt EM, Boone JM. The essential physics of medical imaging. Philadelphia, PA: Lippincott Williams & Wilkins; 2001.

23. Goodsitt MM, Christodoulou EG, Larson SC. Accuracies of the synthesized monochromatic CT numbers and effective atomic numbers obtained with a rapid kVp switching dual energy CT scanner. Med Phys. 2011;38(4):2222–32.

24. Vetter J and Holden J. Correction for scattered radiation and other background signals in dual-energy computed tomography material thickness measurements. Med Phys. 1988;15(5):726–31.

25. Cardinal HN and Fenster A. An accurate method for direct dual-energy calibration and decomposition. Med Phys. 1990;17(3):327–41.

26. Primak A, Ramirez Giraldo JC, Liu X, Yu L, McCollough C. Improved dual-energy material discrimination for dual-source CT by means of additional spectral filtration. Med Phys. 2009;36(4):1359–69.

27. Yang M, Virshup G, Clayton J, Zhu X, Mohan R, Dong L. Does kV–MV dual-energy computed tomography have an advantage in determining proton stopping power ratios in patients? Phys Med Biol. 2011;56(14):4499–515.

28. Zhang D, Li XH, Liu B. Objective characterization of GE Discovery CT750 HD scanner: gemstone spectral imaging mode. Med Phys. 2011;38(3):1178–88.

29. Papanikolaou N, Battista J, Boyer A, et al. Tissue inhomogeneity corrections for megavoltage photon beams. AAPM Task Group 65. Madison (WI): Medical Physics Publishing; 2004.

30. Venselaar J, Welleweerd H, Mijnheer B. Tolerances for the accuracy of photon beam dose calculations of treatment planning systems. Radiother Oncol. 2001;60(2):191–201.

31. Joseph PM and Spital RD. The effects of scatter in x-ray computed tomography. Med Phys. 1982;9(4):464–72.

32. Petit SF, van Elmpt WJC, Nijsten SM, Lambin P, Dekker AL. Calibration of megavoltage cone-beam CT for radiotherapy dose calculations: correction of cupping artifacts and conversion of CT numbers to electron density. Med Phys. 2008;35(3):849–65.

33. Morin O, Chen J, Aubin M, et al. Dose calculation using megavoltage cone-beam CT. Int J Radiat Oncol Biol Phys. 2007;67(4):1201–10.

RADIATION
ONCOLOGY

SHORT REPORT   **Open Access**

Feasibility and accuracy of relative electron density determined by virtual monochromatic CT value subtraction at two different energies using the gemstone spectral imaging

Toshiyuki Ogata[1]*, Takashi Ueguchi[1], Masashi Yagi[2], Sachiko Yamada[1], Chikako Tanaka[1], Ryota Ogihara[1], Fumiaki Isohashi[2], Yasuo Yoshioka[2], Noriyuki Tomiyama[3], Kazuhiko Ogawa[2] and Masahiko Koizumi[4]

Abstract

Background: Recent work by Saito (2012) has demonstrated a simple conversion from energy-subtracted computed tomography (CT) values (ΔHU) obtained using dual-energy CT to relative electron density (RED) via a single linear relationship. The purpose of this study was to investigate the feasibility of this method to obtain RED from virtual monochromatic CT images obtained by the gemstone spectral imaging (GSI) mode with fast-kVp switching.

Methods: A tissue characterization phantom with 13 inserts made of different materials was scanned using the GSI mode on a Discovery CT750 HD. Four sets of virtual monochromatic CT images (60, 77, 100 and 140 keV) were obtained from a single GSI acquisition. When we define Δ HU in terms of the weighting factor for the subtraction a, $\Delta HU \equiv (1 + a)H - aL$ (H and L represent the CT values for high and low energy respectively), the relationship between Δ HU and RED is approximated as a linear function, $a \times \Delta HU/1000 + b$ (a, b = unity). We evaluated the agreement between the determined and nominal RED. We also have investigated reproducibility over short and long time periods.

Results: For the 13 insert materials, the RED determined by monochromatic CT images agreed with the nominal values within 1.1% and the coefficient of determination for this calculation formula was greater than 0.999. The observed reproducibility (1 standard deviation) of calculation error was within 0.5% for all materials.

Conclusions: These findings indicate that virtual monochromatic CT scans at two different energies using GSI mode can provide an accurate method for estimating RED.

Keywords: Gemstone spectral imaging, Monochromatic images, Relative electron density, Dual energy, Computed tomography

Introduction

Computed tomography (CT) images are used as fundamental input data for most modern radiotherapy treatment planning systems. CT data not only provide anatomic information to delineate target volumes and organs at risk, but also apply corrections to dose calculation to account for tissue inhomogeneities during the radiation

treatment planning procedure. These corrections are based on the determination of a relationship between the tissue electron density and its corresponding Hounsfield units (HU) [1].

Dual energy CT (DECT) is one of the most promising imaging techniques with potential clinical applications [2]. DECT has two major advantages compared with conventional single-source CT systems. First, this modality makes it possible to obtain virtual monochromatic images at an arbitrary energy and improved material decomposition such as the separation of iodine from the

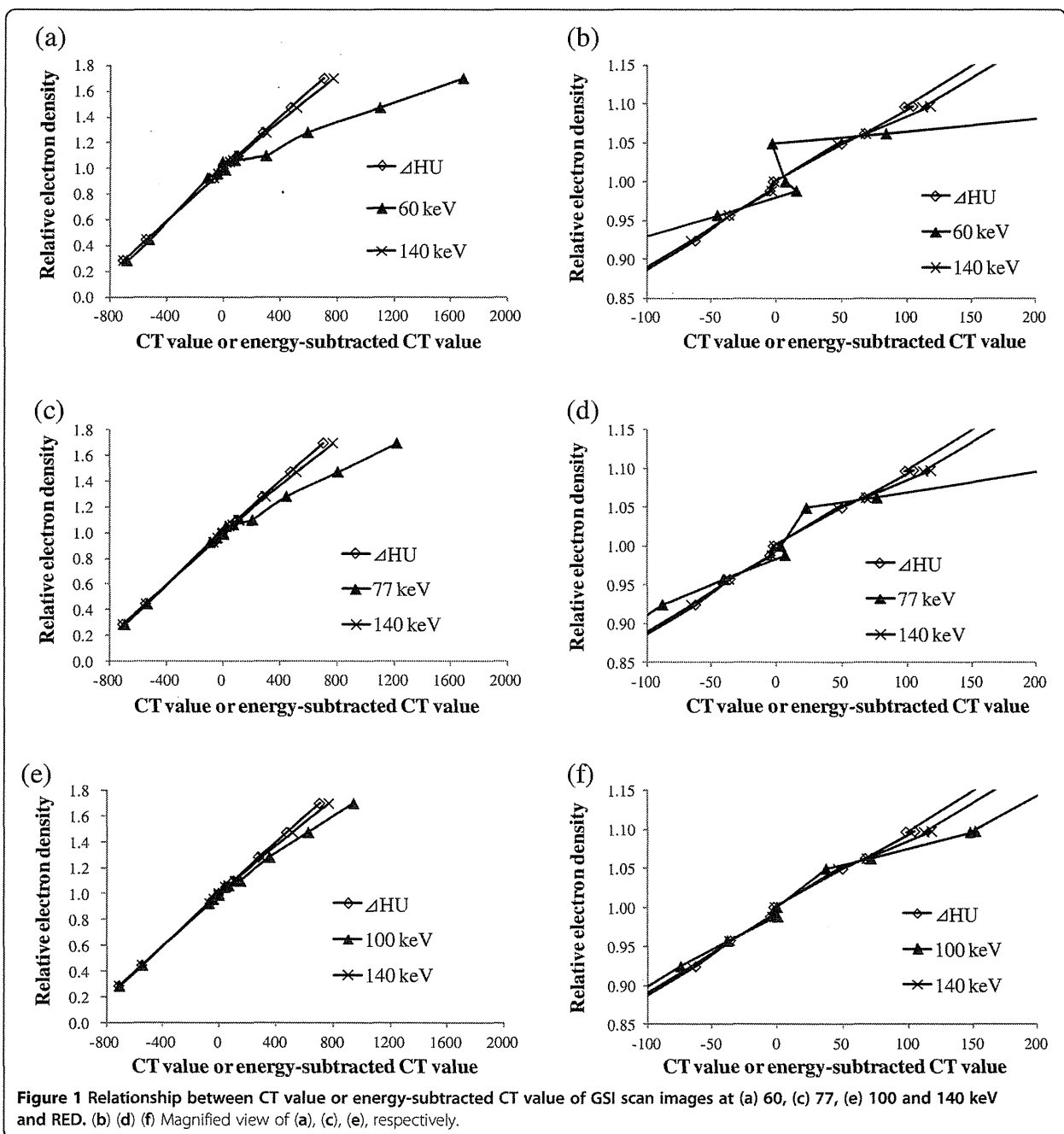* Correspondence: ogata@k-mcc.net
[1]Department of Radiology, Osaka University Hospital, 2-15 Yamadaoka, Suita, Osaka, Japan
Full list of author information is available at the end of the article

image [3]. Second, this modality can reduce beam hardening artifacts [4]. A CT value obtained by conventional CT using polychromatic x-rays could have greater uncertainty because of this beam hardening effect [5].

Saito demonstrated a simple conversion from the energy-subtracted CT values (ΔHU) obtained by DECT to the relative electron density (RED) via a single linear relationship [6]. His method is quite simple and accurate, but it requires polychromatic images at different tube potentials. This could limit its application for some dual-energy strategies in which polychromatic dual-energy images are not available. The purpose of this study is to investigate the feasibility of this method to obtain RED from virtual monochromatic images obtained by the gemstone spectral imaging (GSI) mode with rapid kVp-switching single-source DECT. Rapid kVp-switching single-source DECT is capable of alternating hundreds of times per second between low and high (80 and 140 kVp, respectively) tube

Figure 1 Relationship between CT value or energy-subtracted CT value of GSI scan images at (a) 60, (c) 77, (e) 100 and 140 keV and RED. (b) (d) (f) Magnified view of (a), (c), (e), respectively.

voltage. This DECT has a new garnet crystal scintillator detector with a much faster optical response compared to typical gadolinium-oxysulfide CT detectors [7]. Since reproducibility of the determined RED is an indicator of the CT value integrity and a prerequisite for radiation therapy treatment, we also investigated the reproducibility of this method over short and long time periods.

Materials and methods

Dual energy CT acquisition

In this study, a rapid kVp-switching single-source DECT (Discovery CT750 HD scanner, GE Healthcare, Milwaukee, WI) was used to obtain virtual monochromatic images. A tissue characterization phantom Gammex 467 (Gammex Inc., Middleton, WI) with 13 inserts made of different materials was scanned. The CT scan was performed with the following parameters: 1.0-second tube rotation, 600 mAs tube current, 2.5 mm slice thickness, and 50 cm field of view. We used four sets of monochromatic images at 60 (relatively low), 77, 100 and 140 keV (highest). The 77 keV was close to the effective energy of a 120 kVp polychromatic x-ray according to the specification. The monochromatic and 120 kVp polychromatic images were reconstructed using GSI and Regular mode, respectively. The method by which the GE scanner synthesizes monochromatic CT values from material density images has been described in detail elsewhere [8]. Monochromatic CT image is obtained from the mass attenuation coefficients and density images of the two basis materials with a normalization process by water attenuation coefficient for the desired energy. This study was conducted under the regulations of the Institutional Review Board of our institution.

Simulation

The dual-energy subtraction for converting CT numbers to RED method developed by Saito [6] was used in this study. According to this method, RED can be calculated simply using CT images at two different energies as follows:

$$a \times \Delta HU/1000 + b,$$

where ΔHU is a dual-energy subtracted quantity defined as $(1 + \alpha)H - \alpha L$ (where α is the weighing factor for the subtraction, and H and L represent the CT values for high and low energy respectively), and a and b are unity. The mean CT numbers in HU were measured for each region of interest using ImageJ software (National Institute of Health, Maryland).

Short-term and long-term reproducibility were evaluated by repeating the same measurement every two hours between 9 AM to 5 PM and performing five additional scans at 1-week intervals. The standard deviation of the error in the obtained relative electron density in

five successive measurements was calculated and used to evaluate the reproducibility.

Statistical methods

The difference in RED between nominal and calculated value by DECT was calculated using the following formula: (calculated value-nominal value)/nominal value × 100. For short-term and long-term reproducibility evaluation, each value is presented as a mean error in RED ± standard deviation.

Results

Figure 1 shows the relationship between the CT value or energy-subtracted CT value of the GSI scan images and RED. The relationship between the CT and RED became more linear with increasing radiation energy. The relationship between the ΔHU of the GSI scan images and RED was found to be linear with the determination coefficient R^2 being greater than 0.999. The obtained a and b ranged from 1.004-1.008 and 0.993-0.999, respectively, indicating that these values are close to unity.
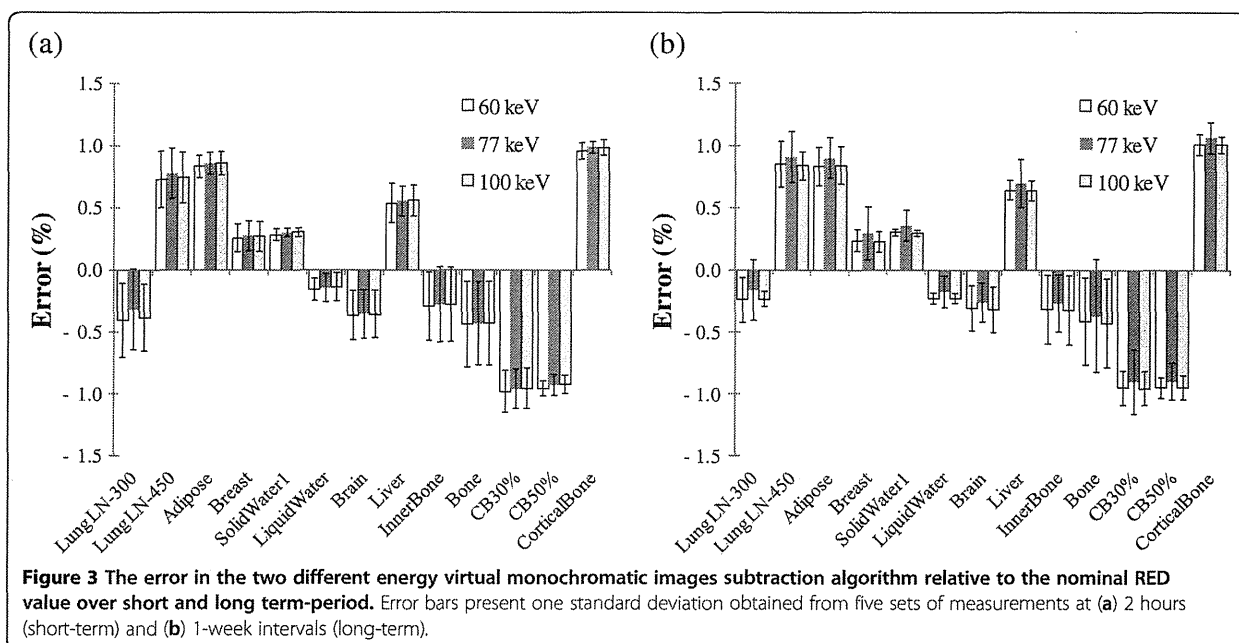
The error in the RED determined by the monochromatic CT scan value subtraction at two different energies using GSI relative to the nominal value is shown in Figure 2. The RED obtained from GSI measurements shows ±1.1% agreement with the nominal values for all inserts. The errors in the two different energy monochromatic images subtraction algorithm relative to the nominal value did not show any energy dependence for low kV scans.

Figure 3 represents the standard deviation for calculation error over short and long time periods. The standard deviation of calculation error over short and long time periods was less than 0.5% for all materials. The reproducibility of the five scans taken at 1-week intervals
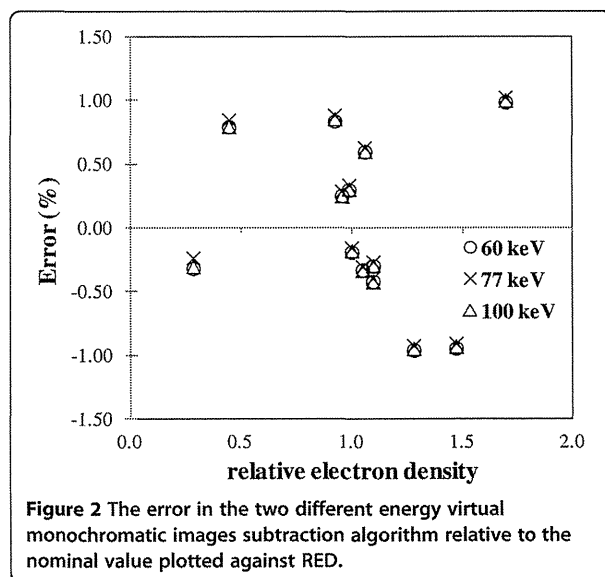
Figure 2 The error in the two different energy virtual monochromatic images subtraction algorithm relative to the nominal value plotted against RED.

Figure 3 The error in the two different energy virtual monochromatic images subtraction algorithm relative to the nominal RED value over short and long term-period. Error bars present one standard deviation obtained from five sets of measurements at (a) 2 hours (short-term) and (b) 1-week intervals (long-term).

was comparable to that of the five scans taken at two-hour intervals. The results showed a standard deviation of 0.02 - 0.45; hence, the long-term reproducibility was as good as the short-term reproducibility. The observed calculation error reproducibility was nearly independent of the radiation energy for low kV scans.

Discussion

Several studies have determined electron density and effective atomic number using the DECT technique [9,10]. However, a practicable dual-energy method that can precisely calculate electron density has not yet been established. We investigated the accuracy of RED obtained by the GSI mode with rapid kVp-switching single-source DECT using the algorithm developed by Saito [6], which is a simple method that converts ΔHU to RED. An advantage of this is that we do not need a priori knowledge regarding the detected x-ray spectra of the CT scanners. We confirmed that the RED obtained from GSI measurements show around ±1.0% agreement with the nominal values for all inserts. IPEM 81 recommends that agreement for electron density should be within 1% for water and within 2% for lung and bone compared with their true values [11]. Agreement for determined RED in our study satisfied the IPEM 81 tolerance levels. These errors are comparable to those of Saito who used a dual-source DECT. The advantages of fast kVp switching CT systems are precise temporal view registration, helical and axial scan, and a 50 cm field of view compared to dual-source DECT [12].

We also investigated the reproducibility of the determined RED over short and long time periods because it is a prerequisite for accurate dose calculations. In the

1980s, the DECT technique had not been used widely in clinical situations due to its lower spatial resolution, unstable CT values, and insufficient tube currents at the low tube voltages of the early CT scanners [13]. We observed that one standard deviation of calculation error was within 0.5% for all materials over the short and long time periods, indicating that no significant variation was observed over the time of the study.

We recognize several limitations in our study. First, we did not evaluate the dependence on scan object size which influences the beam hardening effect. Saito examined the effect of object size on converting ΔHU to RED and confirmed no dependence on the object size [6]. Second, we did not scan high electron density metal, which significantly affects dose distribution in radiation treatment. Further intensive studies are needed to confirm the feasibility of this method for converting ΔHU to RED when using virtual monochromatic images obtained by the GSI mode.

In conclusion, a virtual monochromatic CT scan at two different energies using the GSI mode provides an accurate method for estimating RED.

Authors' contributions
TO performed experiments and drafted the manuscript. TU conceived of the study and participated in its design and coordination and helped to draft the manuscript. MY, SY, RO, and CT collected the data and performed the data analysis. FI, YY, NT, MK, and KO helped to finalize the manuscript. All authors read and approved the final manuscript.

Author details
[1]Department of Radiology, Osaka University Hospital, 2-15 Yamadaoka, Suita, Osaka, Japan. [2]Department of Radiation Oncology, Osaka University Graduate School of Medicine, 2-2 Yamadaoka, Suita, Osaka, Japan. [3]Department of Radiology, Osaka University Graduate School of Medicine, 2-2 Yamadaoka, Suita, Osaka, Japan. [4]Division of Medical Physics, Oncology Center, Osaka University Hospital, 2-15 Yamadaoka, Suita, Osaka, Japan.

References
1. Constantinou C, Harrington JC, DeWerd LA: An electron density calibration phantom for CT-based treatment planning computers. *Med Phys* 1992, 19:325–327.
2. Karçaaltıncaba M, Aktaş A: Dual-energy CT revisited with multidetector CT: review of principles and clinical applications. *Diagn Interv Radiol* 2011, 17:181–194.
3. Johnson TR, Krauss B, Sedlmair M, Grasruck M, Bruder H, Morhard D, Fink C, Weckbach S, Lenhard M, Schmidt B, Flohr T, Reiser MF, Becker CR: Material differentiation by dual energy CT: initial experience. *Eur Radiol* 2007, 17:1510–1517.
4. Bamberg F, Dierks A, Nikolaou K, Reiser MF, Becker CR, Johnson TR: Metal artifact reduction by dual energy computed tomography using monoenergetic extrapolation. *Eur Radiol* 2011, 21:1424–1449.
5. Torikoshi M, Tsunoo T, Sasaki M, Endo M, Noda Y, Ohno Y, Kohno T, Hyodo K, Uesugi K, Yagi N: Electron density measurement with dual-energy x-ray CT using synchrotron radiation. *Phys Med Biol* 2003, 48:673–685.
6. Saito M: Potential of dual-energy subtraction for converting CT numbers to electron density based on a single linear relationship. *Med Phys* 2012, 39:2021–2030.
7. Ko JP, Brandman S, Stember J, Naidich DP: Dual-energy computed tomography: concepts, performance, and thoracic applications. *J Thorac Imaging* 2012, 27:7–22.
8. Goodsitt MM, Christodoulou EG, Larson SC: Accuracies of the synthesized monochromatic CT numbers and effective atomic numbers obtained with a rapid kVp switching dual energy CT scanner. *Med Phys* 2011, 38:2222–2232.
9. Bazalova M, Carrier JF, Beaulieu L, Verhaegen F: Dual-energy CT-based material extraction for tissue segmentation in Monte Carlo dose calculations. *Phys Med Biol* 2008, 53:2439–2456.
10. Landry G, Reniers B, Granton PV, van Rooijen B, Beaulieu L, Wildberger JE, Verhaegen F: Extracting atomic numbers and electron densities from a dual source dual energy CT scanner: experiments and a simulation model. *Radiother Oncol* 2011, 100:375–379.
11. Mayles WPH, Lake R, Mckenzie A, Macauley EM, Morgan HM, Jordan TJ, Powley SK: *Physics aspects of quality control in radiotherapy IPEM Report 81.* The Institute of Physics and Engineering in Medicine; 1999.
12. Geyer LL, Scherr M, Körner M, Wirth S, Deak P, Reiser MF, Linsenmaier U: Imaging of acute pulmonary embolism using a dual energy CT system with rapid kVp switching: Initial results. *Eur J Radiol* 2012, 81:3711–3718.
13. Fletcher JG, Takahashi N, Hartman R, Guimaraes L, Huprich JE, Hough DM, Yu L, McCollough CH: Dual-energy and dual-source CT: is there a role in the abdomen and pelvis? *Radiol Clin North Am* 2009, 47:41–57.

High dose rate brachytherapy for oral cancer

Hideya YAMAZAKI[1,*], Ken YOSHIDA[2], Yasuo YOSHIOKA[3], Kimishige SHIMIZUTANI[3],
Souhei FURUKAWA[4], Masahiko KOIZUMI[3] and Kazuhiko OGAWA[3]

[1]Department of Radiology, Kyoto Prefectural University of Medicine, 465 Kajiicho Kawaramachi Hirokoji, Kamigyo-ku,
Kyoto 602-8566, Japan
[2]Department of Radiology, National Hospital Organization, Osaka National Hospital, Hoenzaka 2-1-14 Chuo-ku,
Osaka City, Osaka 540-0006, Japan
[3]Department of Radiation Oncology, Osaka University Graduate School of Medicine, Yamadaoka 2-2, Suita, 565-0871
Osaka, Japan
[4]Department of Maxillo-Facial Radiology, Osaka University Graduate School of Densitry, Yamadaoka 1-8, Suita, 565-0871
Osaka, Japan
*Corresponding author. Department of Radiology, Kyoto Prefectural University of Medicine, 465 Kajiicho Kawaramachi
Hirokoji, Kamigyo-ku, Kyoto 602-8566, Japan. Tel: +81-75-251-5618; Fax: +81-75-251-5840; Email: hideya10@hotmail.com

Brachytherapy results in better dose distribution compared with other treatments because of steep dose reduction in the surrounding normal tissues. Excellent local control rates and acceptable side effects have been demonstrated with brachytherapy as a sole treatment modality, a postoperative method, and a method of reirradiation. Low-dose-rate (LDR) brachytherapy has been employed worldwide for its superior outcome. With the advent of technology, high-dose-rate (HDR) brachytherapy has enabled health care providers to avoid radiation exposure. This therapy has been used for treating many types of cancer such as gynecological cancer, breast cancer, and prostate cancer. However, LDR and pulsed-dose-rate interstitial brachytherapies have been mainstays for head and neck cancer. HDR brachytherapy has not become widely used in the radiotherapy community for treating head and neck cancer because of lack of experience and biological concerns. On the other hand, because HDR brachytherapy is less time-consuming, treatment can occasionally be administered on an outpatient basis. For the convenience and safety of patients and medical staff, HDR brachytherapy should be explored. To enhance the role of this therapy in treatment of head and neck lesions, we have reviewed its outcomes with oral cancer, including Phase I/II to Phase III studies, evaluating this technique in terms of safety and efficacy. In particular, our studies have shown that superficial tumors can be treated using a non-invasive mold technique on an outpatient basis without adverse reactions. The next generation of image-guided brachytherapy using HDR has been discussed. In conclusion, although concrete evidence is yet to be produced with a sophisticated study in a reproducible manner, HDR brachytherapy remains an important option for treatment of oral cancer.

Keywords: brachytherapy; oral cancer; high dose rate

INTRODUCTION

Because adjacent normal tissues, such as the salivary glands, mandible, and mastication muscles, are at risk of damage during treatment with external beam radiation therapy (EBRT), brachytherapy is an important alternative to conventional radiotherapy. Brachytherapy provides a high localized dose of radiation, with rapid fall-off and short overall treatment time [1]. It can be applied as a sole treatment, as a treatment complementary to surgery, and as a local boost in combination with EBRT.

Low-dose-rate (LDR) brachytherapy has been employed in the treatment of carcinoma of the lip, tongue, floor of the mouth, oral mucosa, base of the tongue, tonsillar region, soft palate, and nasopharynx, and has been the gold standard for brachytherapy. With the advent of new

technologies, high-dose-rate (HDR) and pulsed-dose-rate (PDR) brachytherapy have been adapted in many institutes to avoid exposure of health care providers to radiation. HDR and PDR stepping source technology offer the advantage of optimizing dose distribution by varying dwell times [1]. The application of HDR brachytherapy has expanded to many sites, having been used in treatment of gynecological cancer, breast cancer, and prostate cancer [2, 3]. Guedea et al. reported that gynecological brachytherapy remains the most common application, although the use of brachytherapy in prostate cancer and breast cancer has increased in Europe [4].

CT-based dosimetry has become increasingly common since 2002. Use of HDR and PDR techniques has increased markedly, while use of both LDR and medium-dose-rate brachytherapy has declined. However, for head and neck cancer, HDR usage decreased in Group I institutes (those in countries with the highest GDP) from 5% (2002) to 2% (2007) [4]. LDR and PDR interstitial brachytherapies (ISBT) were utilized instead. Accordingly, HDR brachytherapy has not become widely used in the radiotherapy community for treating head and neck cancer because of lack of experience and biological concerns [5, 6].

Mazeron et al. noted that the efficacy and safety of HDR brachytherapy must be validated in prospective studies. If it is the only technique available, treatment should be delivered in fractions of <3–4 Gy, according to GEC-ESTRO recommendations [1]. Several members of the American Brachytherapy Society expressed concern about potential morbidity with fraction sizes as large as 6 Gy to the oral cavity [6]. On the other hand, very little clinical evidence has been found suggesting a higher risk of high-dose fractionation (≥6 Gy). Acceptable results have been obtained from a few institutes.

To enhance the role of HDR brachytherapy, we reviewed the results of HDR brachytherapy, including our experiences in Phase I/II and III trials, to investigate the next generation of image-guided brachytherapy using HDR.

HDR brachytherapy for tongue cancer

Tongue cancer located anterior to the circumvallate papillae vitally affects not only speech, but also coordination of chewing and swallowing. Because radiation therapy is considered to be a minimally invasive treatment procedure, it has the advantage of preserving the shape and functions of the tongue. Brachytherapy alone is recommended for T1N0 and T2N0 tumors <4 cm. For tumors >3–4 cm or N1 lesions, although surgery is often preferred, brachytherapy can be delivered as a boost after 40–45 Gy of EBRT to the neck and oral cavity. In general, the local control rate is higher than 90% for T1 and T2N0 tumors treated with LDR brachytherapy alone [1]. The local control rate is lower in patients with larger tumors treated with EBRT and a brachytherapy boost. Approximately 10–30% of patients

may develop soft tissue necrosis within the implant volume. Osteoradionecrosis may occur in 5–10% of cases. The vast majority of necroses heal spontaneously after medical treatment. Surgical intervention is necessary in only 1–2% of patients [1].

Lau et al. initiated a Phase I/II protocol using HDR-ISBT [7] (Table 1). In that study, 27 patients were treated (T1, n = 10; T2, n = 15; and T3, n = 2). Seven fractions × 6.5 Gy of HDR-ISBT were administered twice-daily, with a minimum interval time of 6 h over a period of 3.5 days. The actual tumor control probability after HDR brachytherapy was 53% at 5 years. Local control rates for T1 and T2 tumors were lower than those for comparable historical controls treated at our institution using LDR radium (Ra-226) or cesium (Cs-137) needle implants and iridium (Ir-192) wire implants. In addition, a trend was observed toward a higher incidence of severe complications for HDR patients compared with the historical controls treated with LDR brachytherapy.

On the other hand, Leung et al. reported good outcomes for eight patients treated solely with HDR-ISBT. Five patients had T1N0 disease, and the remaining three had T2N0 disease [8]. The median follow-up period for these patients was 26 months. The median dose administered was 60 Gy/10 fractions over 6 days. Mandibular and maxillary shields were inserted prior to treatment. Mucositis for 6–20 weeks (median, 10 weeks) was observed in all patients. No local failure was evident after the median follow-up period. One patient treated with a double planar implant developed Grade 3 necrosis of the soft tissue and bone. Leung et al. [8] concluded that the HDR remote after-loading technique is useful because it provides a local control rate of 100% with acceptable morbidity. On further investigation in 2002, they found that a protocol of 5.5 Gy/10 fractions was feasible, resulting in a local control rate of 94% at 4 years in ten T1 and nine T2 patients without severe morbidity [9].

Ohga et al. treated 28 patients with N0 oral tongue cancer using HDR-ISBT combined with local injection of bleomycin [10]. A median dose of 5 mg bleomycin was injected locally, and 16–20 Gy was delivered to the area surrounding the applicators within the first two days for control of the tumor implant. The 2-year local recurrence-free survival rate in that study was 96% [T1/2: 100% (8/8, 15/15); T3: 80% (4/5)]. The minimum tumor dose was decreased step-by-step. Local recurrence rates of 12.5% (1/8), 0% (0/14), and 0% (0/6) were observed in patients with median minimum tumor doses of 60, 50 and 40 Gy, respectively. Local recurrence rates did not increase when the minimum tumor dose decreased. Late adverse effects included the following: tongue ulcer (11%, 3/28), oral floor ulcer (4%, 1/28), and osteonecrosis (4%, 1/28). These results suggest that decrease in the minimum tumor dose to <60 Gy may be possible in combination treatment with local injection of bleomycin.